

# The protein matrix of plastocyanin supports long-distance charge transport with photosystem I and the copper ion regulates its spatial span and conductance

Manuel López-Ortiz,<sup>†1,2</sup> Ricardo A. Zamora,<sup>†1,2</sup> Marina I. Giannotti,<sup>1,2,3</sup> and Pau Gorostiza<sup>1,2,4\*</sup>

1. Institute for Bioengineering of Catalonia (IBEC), The Barcelona Institute of Science and Technology, Baldiri Reixac 10–12, Barcelona 08028, Spain

2. CIBER-BBN, ISCIII, Barcelona, Spain

3. Department of Materials Science and Physical Chemistry, University of Barcelona, Martí i Franquès 1-11, Barcelona 08028, Spain

4. Catalan Institution for Research and Advanced Studies (ICREA), Barcelona 08010, Spain

\* E-mail: pau@icrea.cat

† These authors contributed equally to this work.

Keywords: interprotein electron transfer, single molecule measurements, cupredoxin, blue copper protein, redox-active site, redox protein, encounter complex, electrochemical tunneling microscopy, current distance spectroscopy, blinking, protein conductance, Gouy-Chapman conduit.

Charge exchange is the fundamental process that sustains cellular respiration and photosynthesis by shuttling electrons in a cascade of electron transfer (ET) steps between redox cofactors. While intraprotein charge exchange is well characterized in protein complexes bearing multiple redox sites, interprotein processes are less understood due to the lack of suitable experimental approaches and the dynamic nature of the interactions. Proteins constrained between electrodes are known to support electron transport (ETp) through the protein matrix even without redox cofactors, as the charges housed by redox sites in ET are furnished by the electrodes in ETp configuration. However, it is unknown whether protein ETp mechanisms apply to the interprotein medium that is present in physiological conditions. Here, we study interprotein charge exchange between plant photosystem I (PSI) and its soluble redox partner plastocyanin (Pc) and address the role of the Pc copper center. Using electrochemical scanning tunnelling spectroscopy (ECSTS) current-distance and blinking measurements we respectively quantify the spatial span of charge exchange between individual Pc/PSI pairs and ETp through transient Pc/PSI complexes. Pc devoid of the redox center ( $Pc_{apo}$ ) can exchange charge with PSI and it does so at longer distances than with the copper ion ( $Pc_{holo}$ ). Conductance bursts associated to  $Pc_{apo}$ /PSI complex formation are higher than in  $Pc_{holo}$ /PSI. Thus, copper ions are not required for long distance ETp between PSI and Pc but regulate its spatial span and conductance. Our results suggest that the redox center that carries the charge in Pc is not necessary to exchange it in interprotein ET through the aqueous solution, and question the canonical view of tight complex binding between redox protein partners.

## Introduction

Three canonical steps are involved in interprotein charge exchange:<sup>1</sup> diffusion of the charge-exchanging proteins, transient complex formation, and electron transfer (ET). Describing the latter, the tunnelling mechanism predicts efficient ET rates for distances below 0.15 nm between donor and acceptor cofactors.<sup>2</sup> In the photosynthetic electron transport chain, electrons are transported along several nanometers *via* a cascade of tunnelling steps between neighboring cofactors.<sup>2,3</sup> However, such a mechanism, incoherent hopping, cannot account for experiments of protein electron transport (ETp)<sup>4,5</sup> in which charge transfer is measured through proteins placed in between an electrode pair. In ETp experiments of single proteins,<sup>6-9</sup> few proteins,<sup>10-13</sup> or protein monolayers,<sup>14-16</sup> electrodes provide an electron source and drain. Thus, ETp does not require the presence of redox cofactors to transport charge<sup>6,10,17</sup> whereas such molecular electronic states are ineluctable steppingstones in ET. The observation of ETp through non-redox proteins<sup>6,10,17</sup> challenges the view of the polypeptide chain as a mere scaffold for redox cofactors and as passive "protein matrix" akin to a low conductance dielectric medium. In addition, temperature independent ETp has been reported for protein junctions wider than 5 nm,<sup>10,14,18</sup> a distance that largely exceeds the tunnelling range.

In previous works we have addressed interprotein ET using an electrochemical scanning tunnelling microscope (ECSTM). We mimic the interprotein ET-like situation facing protein partners bound to electrodes and located at nanometer proximity.<sup>19,20</sup> In this configuration, for a redox cognate pair of the respiratory chain, we measured current at distances as long as 12 nm through the aqueous solution.<sup>19,20</sup> Furthermore, the spatial span of the interprotein current in cytochrome *c* is regulated by phosphorylation,<sup>20</sup> which highlights the biological relevance of this observation. In the absence of a redox chain in the electrolyte solution, such observations require a different mechanism than ET in the bound complex,<sup>21</sup> raising several questions: can the ETp mechanisms operating in the polypeptide structures support charge transport between proteins through the solution? are observations of long-distance currents restricted to these cytochrome partners or is it a general phenomenon? does protein recognition, which is essential for interprotein ET,<sup>22-26</sup> play a role in ETp?

We now pose these questions to protein partners of the photosynthetic electron transport chain, photosystem I light harvesting complex I (PSI-LHCI, noted PSI throughout the manuscript for simplicity) and plastocyanin (Pc). In particular, we measure the distance dependence of the charge exchange between PSI and Pc and the conductance of the complex they form using electrochemical scanning tunnelling spectroscopy (ECSTS).<sup>27,28</sup> In the photosynthetic electron transport chain, charge between the membrane bound complexes cytochrome *b<sub>6</sub>f* and PSI is carried by Pc<sup>29</sup> (Figure 1a). Transient spectroscopic measurements<sup>22-26,30-32</sup> tracking Pc/PSI ET exhibit a fast  $\mu$ s phase associated with the ET of preformed complexes and a slower ms phase, dependent on Pc concentration and related to the Pc/PSI complex formation. We have recently studied the binding of single Pc/PSI pairs using force spectroscopy.<sup>33</sup> Controlling the redox state of PSI and Pc, we quantified the binding probability as the number of adhesion events. For Pc/PSI, the binding probability depends on the proteins' redox state and is higher when at least one of the partners is in an ET-ready state.<sup>33</sup> Those results pave the way for disentangling the contribution of binding from the overall charge exchange process between PSI and Pc. However, characterization of the ET step between Pc/PSI pairs is lacking. To fill this gap, we emulate Pc/PSI interprotein ET in ETp configuration. Furthermore, we investigate the intriguing nature of ETp in non-redox proteins using Pc<sub>apo</sub> (devoid of copper ion) and Pc<sub>holo</sub> (with the copper ion in its binding site), to tell apart the contributions of the redox cofactor and of the protein structure, which is similar for Pc<sub>holo</sub> and Pc<sub>apo</sub>.<sup>34</sup> Density functional theory (DFT) based calculations for azurin have shown that in ETp configuration Cu<sup>2+</sup> does not contribute significantly to the junction conductance.<sup>35-37</sup> As reported for Pc, the crystallographic structure of apo and holo azurin are nearly identical, however,

the copper ion in azurin was shown to have a structural function. Experiments of single-molecule mechanical unfolding with an atomic force microscope (AFM) and computer simulations revealed that the metal-binding region is mechanically flexible in apo-azurin.<sup>38</sup> Flexibility in the metal-binding site facilitates the loading of the metal center in azurin allowing to mature into the holo form assisted by metallochaperones *in vivo*, and to gain redox activity upon incubation with  $\text{Cu}^{2+}$  ions *in vitro*.<sup>38</sup>

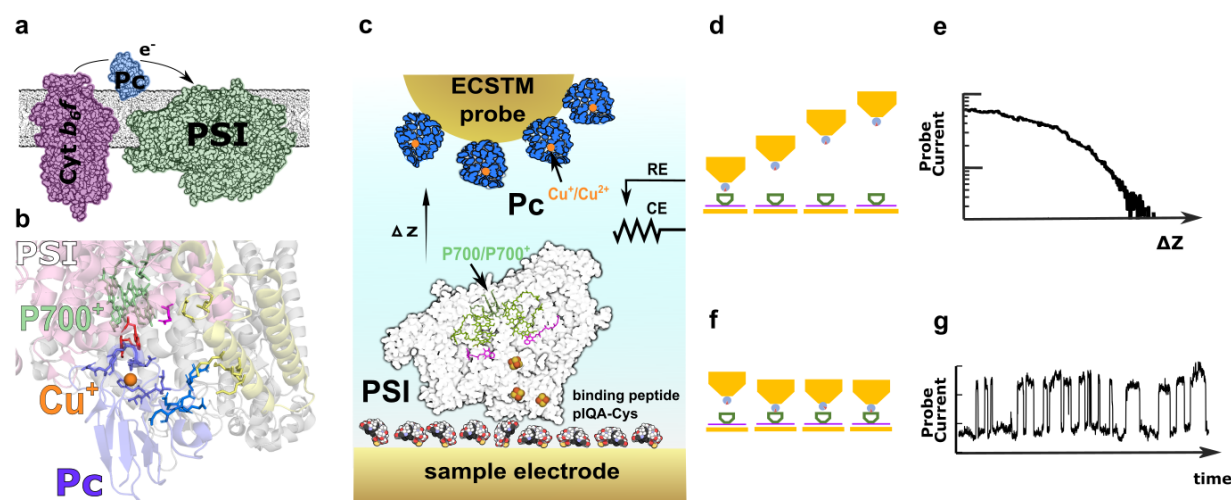


**Figure 1. PSI-LHCI-Pc charge exchange:** (a) Schematic representation of charge exchange between Cyt *b<sub>6</sub>f* (purple) and PSI-LHCI (green) mediated by Pc (blue) in the luminal side of thylakoid membrane. (b) PSI-Pc transient complex structure (6YEZ) in cartoon representation of Pc (blue), PsaA (pink), PsaB (white), and PsaF (yellow) subunits. Redox cofactors are highlighted in green for the P700 pair and in orange for the Cu atom in Pc. Residues with a reported role on PSI-Pc ET are also highlighted: PsaA Trp625, PsaB Trp658 (red), PsaB Glu613 (pink), and PsaF lysines Lys93, Lys96, Lys100, Lys101 (yellow). Pc Residues interacting with PsaA and PsaB are shown in purple and those interacting with PsaF lysines are shown in blue. (c) Experimental set-up of ECSTM distance current decay spectroscopy. PSI-LHCI (white) is functionalized *via* pIQA-cys linker peptide bound to the Au sample electrode. The Pc (blue) functionalized Au probe electrode is retracted perpendicularly to the sample electrode plane (*z* axis). Arrows indicate the redox cofactors, P700/P700<sup>+</sup> and  $\text{Cu}^{+/2+}$  of PSI-LHCI and Pc, respectively. RE and CE represent counter electrode (Pt wire) and reference electrode (low leakage silver-silver chloride SSC), respectively. (d) Scheme depicting current-distance decay spectroscopy experiments. (e) Example of current-distance recording  $I(z)$ . (f) Scheme of blinking experiment. (g) Example recording of blinking events displaying a telegraphic noise signal.

In this work, we aim to tell apart the contribution of charge exchange between cognate proteins from the contributions of diffusion, complex formation, and re-arrangement, by controlling their relative orientation and separation and thus extending ETp measurements to the electrolyte medium.<sup>19</sup> To do so, we orient PSI with a peptide that specifically binds to the PSI stromal side (pIQAcys),<sup>39,40</sup> thereby exposing to the solution the binding site for Pc. The pIQAcys is bound to the sample Au electrode via an introduced cysteine (Figure 1c).<sup>19</sup> The spatial span of the protein charge exchange is assessed by recording the probe current during retraction (Figure 1d) yielding a double-exponential current decay<sup>41,42</sup> (Figure 1e). The current-distance decay rate ( $\beta$ ,  $\text{nm}^{-1}$ ) obtained by fitting current-distance plots is a proxy indicator of the interprotein charge exchange distance.<sup>19,20,40-44</sup> In previous works, we measured  $\beta$  for oriented PSI<sup>40,44</sup> complexes facing a Pt/Ir probe at different probe and sample potential pairs, concluding that the current is gated by the probe potential with a minimal  $\beta$  value (longest charge exchange distance) of  $2 \text{ nm}^{-1}$ . Although  $\beta$  for Pc has not been reported, the gating of  $\beta$  by the sample potential was observed for azurin,<sup>42</sup> which is a Pc analogue. Interestingly, the electrochemical gating effect vanished in redox inactive azurin, in which the Cu atom was substituted by Zn.<sup>42</sup> In addition to current-distance measurements, we investigate ET in the Pc/PSI bound complex with the

"blinking" technique, which records the formation of spontaneous, transient protein junctions between electrodes<sup>9,45-49</sup> (Figure 1f). As the junction is formed, a sharp increase in the current (blink) is observed resulting in a telegraphic noise like signal (Figure 1g). The junction conductance (which is proportional to the current at fixed bias potential) provides valuable information on the protein complex ETp mechanism. For instance, in azurin, single point-site mutations at the docking hydrophobic patch allowed to distinguish Cu-mediated and non-Cu-mediated charge transport mechanisms.<sup>47</sup> Additionally, the duration of blinks allows quantifying the time course of the transient complex. The use of these complementary techniques, ECSTS current distance spectroscopy and blinking, allows characterizing charge exchange at long distances and in bound complexes respectively, and provide a comprehensive view of the charge exchange between PSI and Pc.

## Results and Discussion

### *Current-distance spectroscopy: spatial span of the charge exchange*

Prior to study the charge exchange between PSI and Pc, we first evaluated the current-distance dependence of PSI and Pc separately, as well as the behavior of the PSI recognition peptide (pIQAcys). Figure 2 shows between 2000 and 3000 ECTS current-distance curves and their associated  $\beta$  values at negative bias (-100 mV, with  $U_{\text{probe}} = 100$  mV/SSC and  $U_{\text{sample}} = 200$  mV/SSC, imposing electron flow from probe to sample electrode as in physiological conditions). For the PSI recognition peptide pIQAcys (Figure 2, magenta), the current measured with a bare Au probe reduces abruptly beyond 2 nm, which corresponds to an average  $\beta$  value of  $6 \pm 1$  nm<sup>-1</sup> (average  $\pm$  standard deviation). Compared to the current-distance rate of bare Au electrodes<sup>44</sup> ( $\beta \sim 9$  nm<sup>-1</sup>), the pIQAcys peptide bound to the electrode increases the charge exchange distance. Upon incubation of PSI complexes on the pIQAcys sample (Figure 2, green), the charge exchange distance is further extended, lowering  $\beta$  to  $1.5 \pm 0.1$  nm<sup>-1</sup>. Positive bias (+100 mV,  $U_{\text{probe}} = 100$  mV/SSC and  $U_{\text{sample}} = 0$  mV/SSC, corresponding to hole injection from the probe electrode into the PSI decorated sample electrode) yields  $\beta = 2.2 \pm 0.3$  nm<sup>-1</sup> (Supplementary Figure 1, green), in line with reported results.<sup>40</sup> Differences in  $\beta$  with bias sign indicate that injecting electrons to PSI as it occurs in the photosynthetic electron transport chain, facilitates charge exchange compared to hole injection. Regarding Pc functionalized probes facing the pIQAcys binding peptide on the sample, the obtained  $\beta$  is  $1.1 \pm 0.3$  nm<sup>-1</sup> (Figure 2, red). In this case, no significant differences are observed between positive and negative bias (Supplementary Figure 1, red).

We then performed ECSTS current-distance measurements with the physiological partners Pc<sub>holo</sub>/PSI facing each other on the probe/sample electrodes, respectively (Figure 2, pale red). Interestingly, the interaction of the protein partners, with  $\beta = 1.5 \pm 0.3$  nm<sup>-1</sup>, yields similar charge exchange distance compared to PSI or Pc separately. This observation holds for negative bias (physiological sign) and for positive bias (Supplementary Figure 2).

In order to isolate the contribution of the protein matrix (as purified without the copper ion) to the charge exchange process, we carried out current-distance spectroscopy experiments with Cu-less Pc<sub>apo</sub><sup>13</sup> (Figure 3a). Cyclic voltammetry (CV) recordings of Au electrodes incubated with Pc<sub>apo</sub> (Figure 3b, blue) showed no oxidation or reduction peaks distinctive of redox protein absorbed on an electrode. Upon addition of CuSO<sub>4</sub> 50 mM to the buffer solution (at room temperature for 1 hour) and washout, the CV of Pc<sub>holo</sub> displays characteristic oxidation and reduction peaks (Figure 3a, pale red) that confirm the ability of the Au-attached protein to bind and retain copper ions, thereby acquiring redox functionality. Note that following this method, as-prepared Pc<sub>holo</sub> is in the oxidized form, and

during the ECSTS experiments it is kept at the redox midpoint by the applied probe potential  $U_{\text{probe}} = 100 \text{ mV/SSC}$ .

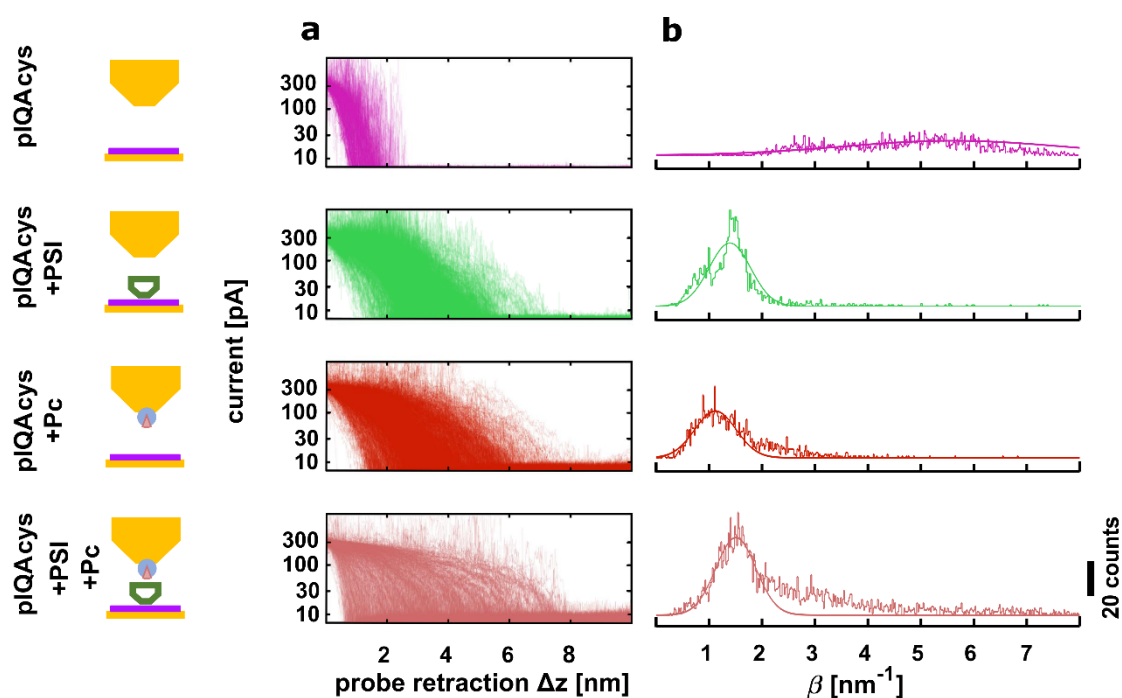


**Figure 2. Current distance spectroscopy of pIQAcys, PSI, Pc and Pc/PSI electrodes.** (a) Raw current-distance  $I(z)$  curves for pIQAcys-Au (magenta) and PSI-pIQAcys-Au (green) samples using a bare Au probe; and samples incubated with pIQAcys-Au (red) and PSI-pIQAcys-Au (pale red) facing a Pc<sub>chole</sub>-Au probe. Each condition is depicted schematically on the left. In all cases,  $n=2000$  curves were recorded in two independent experiments except for Pc/PSI samples that counts three independent experiments ( $n=3000$ ). (b) Current distance rate ( $\beta$ ) histograms obtained using values from  $I(z)$  curves in panel (a) and fit by a normal distribution (solid curve).  $U_{\text{bias}} = -100 \text{ mV}$ ;  $U_{\text{probe}} = 100 \text{ mV/SSC}$ ;  $U_{\text{sample}} = 200 \text{ mV/SSC}$ .

Current-distance spectroscopy of Pc<sub>chole</sub> probes facing pIQAcys-Au electrodes (red, Supplementary Figure 2) yield longer charge exchange distances (lower  $\beta$  values) compared to Cu-less Pc<sub>apo</sub> for both positive and negative bias (black, Supplementary Figure 2). This result indicates that charge exchange between Pc and the gold sample electrode functionalized with pIQAcys peptide (which is not a cognate partner of Pc) is facilitated in the presence of the redox center in Pc, that is, the copper ion enlarges the spatial span of the interaction. Remarkably, facing Pc<sub>apo</sub> to its cognate partner PSI, increases the charge exchange distances, yielding an average  $\beta$  rate of  $0.8 \pm 0.2 \text{ nm}^{-1}$  for negative bias (Figure 3c, pale red) and giving rise to current-distance curves extending up to 8 nm. Strikingly, at negative (physiological) bias,  $\beta$  values between Pc<sub>chole</sub> and PSI ( $1.5 \pm 0.3 \text{ nm}^{-1}$ ) are significantly higher than between Pc<sub>apo</sub> and PSI, indicating that the presence of copper in Pc reduces the charge exchange distance between the partners (Figure 3d). Such decrease in the charge exchange distance between Pc<sub>chole</sub>/PSI compared to Pc<sub>apo</sub>/PSI is not observed at positive bias, which drives electrons from PSI on the sample to Pc on the probe (Supplementary Figure S3). The  $\beta$  values obtained in all the conditions described above are summarized in the Supplementary Information (Supplementary Table ST1).

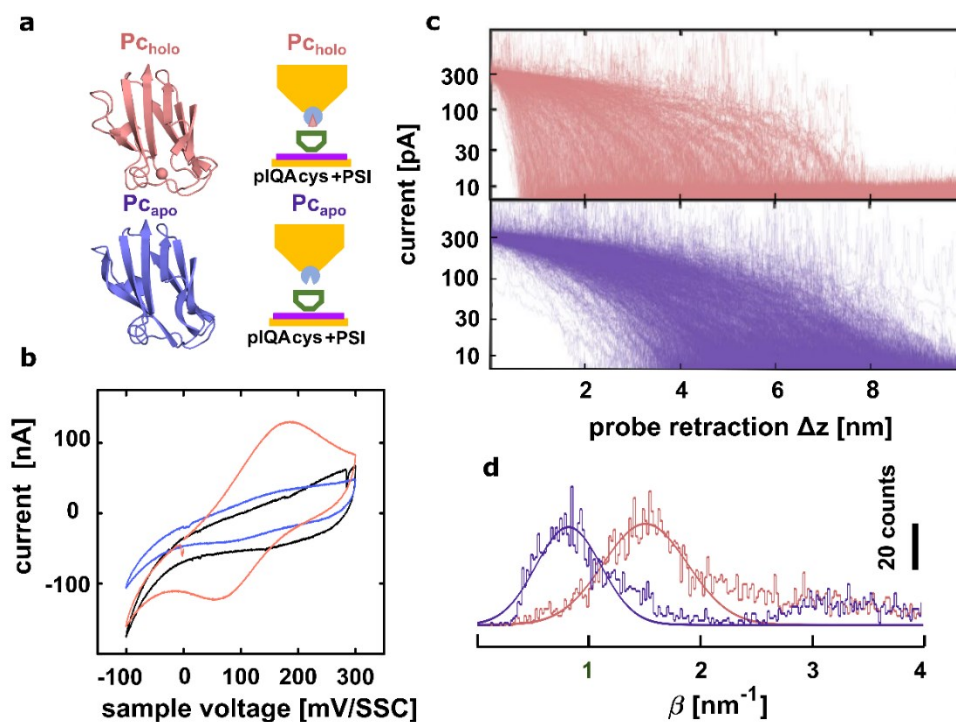


**Figure 3. Preparation of  $Pc_{\text{holo}}$  and  $Pc_{\text{apo}}$ , CV, and ECSTS current-distance spectroscopy of probe-attached  $Pc_{\text{holo}}$  and  $Pc_{\text{apo}}$  facing PSI complexes bound to the sample electrode. (a)** Crystallographic structure of poplar  $Pc_{\text{holo}}$  in pale red (PDB 1PLC) and  $Pc_{\text{apo}}$  in blue (PDB 2PCY) and schematic representation of  $Pc_{\text{holo}}$ /PSI (top) and  $Pc_{\text{apo}}$ /PSI (bottom) samples. **(b)** CV of bare Au[111] electrode (black), after incubation with as-purified  $Pc_{\text{apo}}$  for 2 hours (blue) and after incubation of  $Pc_{\text{apo}}$ -Au sample with  $\text{CuSO}_4$  ( $Pc_{\text{holo}}$ , pale red). **(c)** Raw ECSTS  $I(z)$  data plots for  $Pc_{\text{holo}}$ /PSI (pale red) and  $Pc_{\text{apo}}$ /PSI (blue) as shown in Figure 2a. **(d)** Current-distance rate ( $\beta$ ) histograms for  $\beta$  values obtained from  $n = 3000$   $I(z)$  curves obtained from three independent experiments of 1000 curves each shown in Figure 3c and fit by normal distribution (solid curve).  $U_{\text{bias}} = -100$  mV;  $U_{\text{probe}} = 100$  mV/SSC;  $U_{\text{sample}} = 200$  mV/SSC.

#### *Blinking: formation of spontaneous Pc/PSI junctions*

In ECSTS blinking experiments,<sup>50</sup> the probe positioning feedback loop is transiently turned off at a desired current setpoint (typically during a few seconds) and the probe current is monitored as molecular junctions are randomly formed in the gap between probe and sample electrodes (functionalized respectively with Pc and PSI in our case). Intermittently switching events described as plateaux, telegraphic noise or “blinks” are observed in the current signal (Figure 4a), indicating the transient formation of a junction. Blinks typically last from a fraction of a ms to tens of ms and display a current increase of 0.2 - 2 nA corresponding to 2.5 - 25 · 10<sup>-5</sup>  $G_0$  for a fixed bias potential of 100 mV, where the conductance jump  $\Delta G = \Delta I / U_{\text{bias}}$  is expressed as a multiple of the conductance quantum  $G_0$ . Collections of blinking events ( $n = 4110$  for  $Pc_{\text{apo}}$ /PSI and  $n = 4216$  for  $Pc_{\text{holo}}$ /PSI, see example traces in Figure 4a) were analyzed to quantify their duration  $\Delta t$  and associated conductance change  $\Delta G$ . They are represented in a 'heat map' two-dimensional histogram of  $\Delta G$  as a function of  $\Delta t$  (Figure 4b). Side and bottom panels show accumulated histograms of  $\Delta G$  and  $\Delta t$  to ease the interpretation.

Two conductance maxima are observed in  $\Delta G - \Delta t$  maps: a low conductance peak of  $1.6 \pm 0.1 \cdot 10^{-5} G_0$  (average  $\pm$  standard error of the mean) for  $Pc_{\text{holo}}/PSI$  and  $3.0 \pm 0.1 \cdot 10^{-5} G_0$  for  $Pc_{\text{apo}}/PSI$  (indicated respectively with a red and a blue circle in the side panels of Figure 4b) and a high conductance peak of  $7.1 \pm 0.1 \cdot 10^{-5} G_0$  for  $Pc_{\text{holo}}/PSI$  and  $10.6 \pm 0.2 \cdot 10^{-5} G_0$  for  $Pc_{\text{apo}}/PSI$  (indicated respectively with a red and a blue star in side panels of Figure 4b). In addition, the high  $\Delta G$  peak has a wider distribution for  $Pc_{\text{apo}}/PSI$  than for  $Pc_{\text{holo}}/PSI$  (the standard deviations of the normal fit of the peaks are  $4.2 \cdot 10^{-5} G_0$  and  $2.5 \cdot 10^{-5} G_0$ , respectively).

The higher  $\Delta G$  observed in the absence of the metal ion ( $Pc_{\text{apo}}/PSI$  in Figure 4b, side panels) is consistent with the lower  $\beta$  values obtained in current-distance measurements (Figures 2-3). Although  $Pc_{\text{apo}}$  cannot undergo redox reactions (see Figure 3b), non-redox proteins sandwiched between electrodes have been recently reported to sustain electron transport up to several nm<sup>18</sup> and exhibit conductance resonance features.<sup>6</sup> Those intriguing results have prompted the proposal of a general mechanism for electron transport in proteins<sup>17</sup> that should also be applicable to apo proteins, as discussed below.

Regarding the kinetics of the blinking events (Figure 4b lower panels), pooling all  $\Delta G$  values yields a similar bi-phasic exponential decay for both  $Pc_{\text{holo}}/PSI$  ( $\tau_{\text{fast}} = 1.4 \pm 0.2$  ms,  $\tau_{\text{slow}} = 18.4 \pm 0.4$  ms) and  $Pc_{\text{apo}}/PSI$  ( $\tau_{\text{fast}} = 1.6 \pm 0.2$  ms,  $\tau_{\text{slow}} = 16.5 \pm 0.6$  ms).  $\tau_{\text{fast}}$  and  $\tau_{\text{slow}}$  and their associated uncertainties, have been obtained by linear fit (black traces in Figure 4b) of the natural logarithm of the number of counts vs  $\Delta t$  for short and long time regimes, respectively. In addition, the time course of the blinks associated to high (\*) and low (o) conductance peaks is displayed at the bottom panel of Figure 4b (red and blue symbols for  $Pc_{\text{apo}}/PSI$  and  $Pc_{\text{holo}}/PSI$ , respectively). The fast phase of blinks can be associated with high frequency switching events that are recognizable in individual traces (Supplementary Figure 4). The conductance of these characteristic features,  $\Delta G \sim 2 \cdot 10^{-5} G_0$ , is compatible with low conductance peaks in  $Pc_{\text{holo}}/PSI$  and  $Pc_{\text{apo}}/PSI$  experiments and a lifetime of  $\sim 1$  ms. Similar  $\Delta G$  and  $\Delta t$  of blinking events observed in electrochemical tunnelling junctions have been attributed to trapping/detrapping of charges at localized electronic states associated to water molecules<sup>51,52</sup> which lowers the electron energy barrier thus increasing conductance. On the other hand, the slow phase of blinks corresponds to the total duration of the blinking event (Figure 4a) which is compatible with the formation of  $Pc/PSI$  transient complexes. Direct comparison of our single molecule experiments with bulk measurements is not straightforward, as the reported ms phase<sup>32</sup> associated with  $Pc/PSI$  complex formation exhibits pseudo-first order kinetics and therefore depends on  $Pc$  concentration. Still, rates ranging from 100 to 3000 s<sup>-1</sup> in transient absorption measurements<sup>32</sup> and from 50 to 400 s<sup>-1</sup> in transient photovoltage measurements<sup>30</sup> match the lifetime of our blinking events ( $1/\tau \approx 60$  s<sup>-1</sup>).

Complementarily to Figure 4, we display in Supplementary Figure 5,  $\Delta G - \Delta t$  histograms for blinking traces recorded at positive bias  $U_{\text{bias}} = 100$  mV that set the electron flow from  $PSI$ -functionalized sample electrode to  $Pc$ -functionalized probes (i.e., against physiological charge exchange between  $PSI$ - $Pc$ ). Comparing conductance histograms for positive and negative bias (Supplementary figure 6) shows that low conductance channels (marked with circles in side panels of Figure 4b) around  $\sim 2 \cdot 10^{-5} G_0$  are also present in positive bias conditions. On the other hand, the high conductance peak of  $Pc_{\text{holo}}/PSI$  at  $\sim 7 \cdot 10^{-5} G_0$  (marked with a star in side panel of Figure 4b) splits in two peaks at  $\sim 5 \cdot 10^{-5} G_0$  and  $\sim 11 \cdot 10^{-5} G_0$  for positive bias. Interestingly, this latter peak  $\sim 11 \cdot 10^{-5} G_0$  in  $Pc_{\text{apo}}/PSI$  coincides with the high conductance peak of  $Pc_{\text{apo}}/PSI$  samples at negative bias that disappears for positive bias.

We interpret that high conductance peak of  $P_{C_{\text{holo}}/PSI}$  at  $\sim 7 \cdot 10^{-5} G_0$  is associated to conductance pathways through the copper ion. Under this view, we associate the  $\sim 5 \cdot 10^{-5} G_0$  peak observed for anti-physiological bias, as a decrease of the conductance pathways through Cu. Complementarily, we associate the  $\sim 11 \cdot 10^{-5} G_0$  present in both anti-physiological bias of  $P_{C_{\text{holo}}/PSI}$  and notably in  $P_{C_{\text{apo}}/PSI}$  to conductance channels related to the protein structure that by-pass the redox center. In  $P_{C_{\text{apo}}/PSI}$  the decreased amplitude of the conductance peak at  $\sim 11 \cdot 10^{-5} G_0$  of anti-physiological with respect to physiological bias might indicate that electrostatic interactions are involved in the protein-mediated conductance channels.

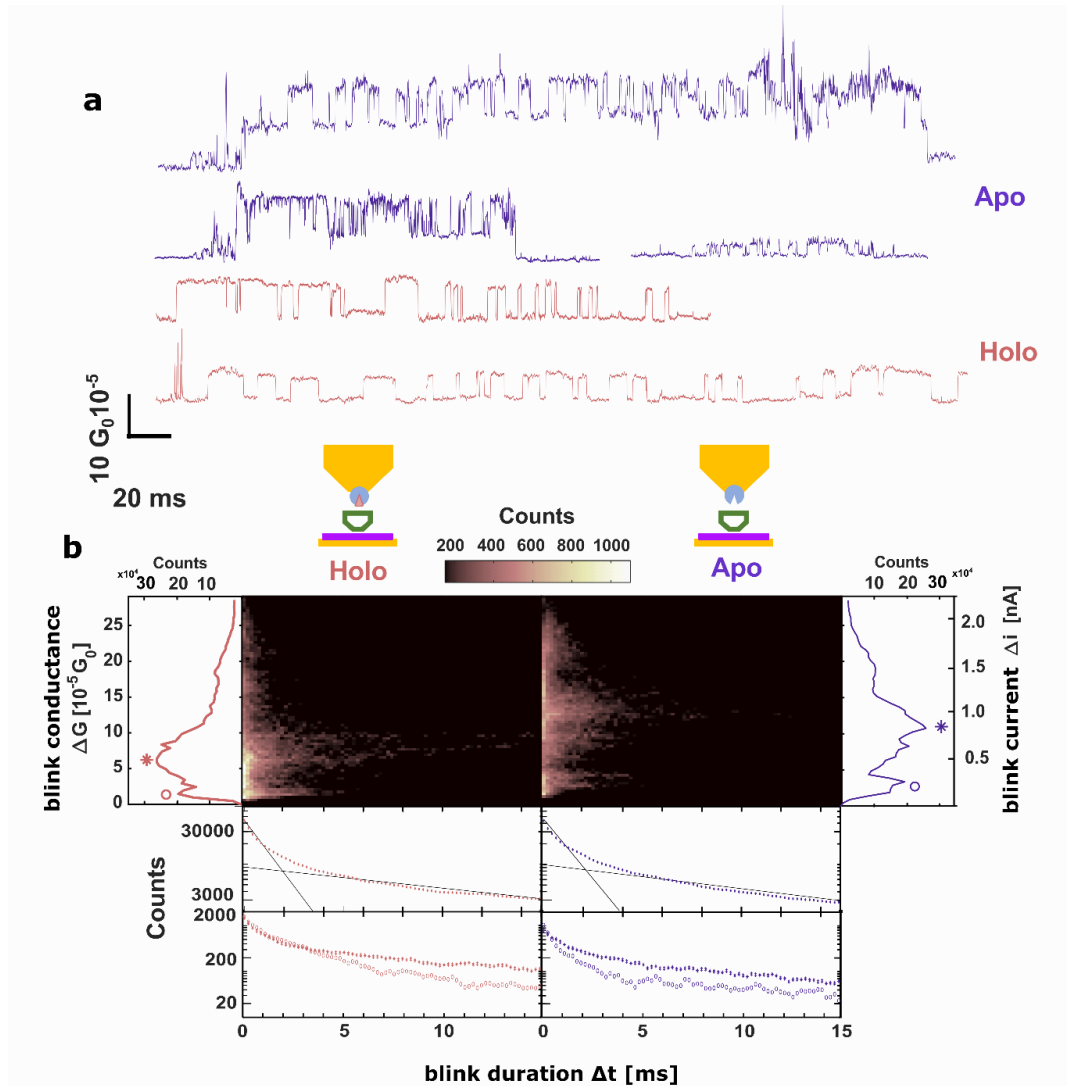


**Figure 4. Blinking recordings in an ECSTM junction with probe-attached  $P_{C_{\text{holo}}}$  and  $P_{C_{\text{apo}}}$  facing PSI complexes on the sample electrode. (a)** Examples of time course of ECSTM probe current at a fixed position in the absence of feedback control. Traces with telegraphic noise features (“blinks”) indicate transient changes in conductance of the junction corresponding to  $P_{C_{\text{holo}}/PSI}$  samples (pale red traces) and bottom to  $P_{C_{\text{apo}}/PSI}$  (blue traces). Set potentials are like current-distance spectroscopy, namely  $U_{\text{probe}} = 100$  mV/SSC,  $U_{\text{sample}} = 200$  mV/SSC, which yield  $U_{\text{bias}} = -100$  mV. **(b)** Blink events ( $n = 4110$  for  $PSI-P_{C_{\text{apo}}}$  and  $n = 4216$  for  $PSI-P_{C_{\text{holo}}}$ ) are pooled together to form a two-dimensional histogram representing the conductance increase of the blink ( $\Delta G$ , left y-axis and  $\Delta i$ , right y-axis), and the duration of the blinking event ( $\Delta t$ , x-axis). Histograms on the side panels show the conductance counts integrated during the time intervals for  $P_{C_{\text{holo}}/PSI}$  in pale red (left) and  $P_{C_{\text{apo}}/PSI}$  in blue (right). Two conductance peaks are present in the histograms, marked with an open circle (O) and an asterisk (\*). The time course of the blinking events is shown in the middle panels under each map after integrating all conductance values. The blinking duration probability,  $P(\Delta t)$ , which is proportional to the number of counts, displays a bi-phasic exponential dependence (thin black lines). For conductance peaks (O and \*), horizontal sections of the  $\Delta G$ - $\Delta t$  map are shown in the bottom panel.

## Discussion

We carried out charge transport measurements between individual partners of the photosynthetic chain (Pc and PSI) and we quantified the contribution of the different components including the redox metal cofactor to the conductance of the junction, its spatial span and time course of interactions. The obtained values in the different experimental conditions are discussed in detail below. Yet, the most striking results are (1) the observation of charge exchange of Pc and PSI at long distances through the aqueous solution, and (2) the ability of copper-less  $Pc_{apo}$  to sustain interprotein ETp with PSI at the single protein level despite the complete absence of redox activity. Our results extend the ETp of non-redox single and monolayer proteins sandwiched between electrodes<sup>6–8,10–18,53</sup> to interprotein charge exchange, providing evidence of ETp between a redox inactive protein and its physiological ET cognate.

From a general perspective, the observation of Pc/PSI interprotein long-distance charge exchange through the solution is akin to results reported previously between protein partners in the respiratory chain<sup>19,20</sup> (cytochrome *c* and complex III, cytochrome *bc*<sub>1</sub>, studied experimentally by means of hCc and pCc<sub>1</sub>). Long distance currents between hCc and pCc<sub>1</sub> are electrochemically gated<sup>19</sup> and regulated by phosphorylation,<sup>20</sup> which indicate the physiological relevance of the process. If the long-range charge exchange observed in ETp configuration takes place in nature, physical (sub nanometric) contact between redox partners would not be a prerequisite for physiological ET.<sup>21</sup> This interpretation raises questions about the underlying mechanism of long distance interprotein charge exchange.<sup>42,43</sup>

To answer them, it seems reasonable to involve the aqueous solution region confined between the proteins, and to avoid explanations based on conventional quantum tunneling since reported charge exchange distances<sup>19,20,40,44</sup> exceed the range accessible by one- and two-step electron tunneling. Longer charge exchange distances are described by thermally activated multi-step mechanisms, however they are incompatible with the available data of temperature independent ETp.<sup>4,5</sup> It has been suggested that electrostatic potential driving ET induces a partial delocalization of the bridge electronic states able to promote long range electron transfer without thermal activation.<sup>54</sup> For the pair hCc/pCc<sub>1</sub>, molecular dynamics calculations revealed a cation depletion region between the interacting partners that hinders charge screening, extending the electric field between redox partners across the electrolyte interface.<sup>19,20</sup> In other words, the cognate partners establish a Gouy-Chapman conduit between them.<sup>19,20</sup> The results presented here support this view, as long distance charge transport (low  $\beta$ ) observed for  $Pc_{apo}$  interacting with PSI is absent when  $Pc_{apo}$  faces a non-cognate sequence like that of the pIQAcys peptide. Remarkably, this extended charge exchange range of  $Pc_{apo}$ /PSI with respect to  $Pc_{holo}$ /PSI is favoured for positive bias, driving electrons from Pc to PSI as it occurs in nature. For the reverse bias,  $\beta$  for  $Pc_{apo}$ /PSI is similar to  $Pc_{holo}$ /PSI which is not affected by the bias sign. Extending the long-distance charge exchange mechanism to the interprotein domain brings up a question: are there intermediate molecular 'bridge' states outside the polypeptide chain and, if so, what is their nature? One possibility is that the localized electronic states identified with charge trapping, associated to low  $\Delta G$  and fast conductance switching features in Figure 4 and Supplementary Figure 4, constitute these intermediate states. Transient configuration of water molecules leading to localized electronic states<sup>52</sup> could mediate interprotein ET as it has been previously suggested.<sup>55–58</sup> Additionally, in *ab initio* electronic structure calculations modelling azurin proteins embedded in a tunnelling junction, it was observed an increase in conductance induced by water molecules enhancing azurin electronic coupling with the electrode.<sup>59</sup>

Regarding the role of the redox center, as  $Pc_{apo}$  is devoid of the metal co-factor it is unable to undergo redox reactions accepting or donating electrons, and thus cannot carry and exchange them with PSI. However, in our ECSTS experiments, the probe and sample electrodes provide an electron source and drain,<sup>4</sup> and therefore we observe that the copper redox center of Pc is not indispensable for ETp through the junction. DFT based calculations in multi-heme cytochrome trapped between electrodes showed that high valence band states associated to the metal contribute poorly to the current.<sup>60</sup> Similar calculations performed with azurin<sup>35,59</sup> incorporating different metal centers and an apo form, revealed that within the coherent transport approach followed by the authors, metal ions do not play a significant role in the conductance.<sup>35</sup> The direct experimental quantification of conductance, blinking, and distance-dependence rates of  $Pc_{apo}/PSI$  and  $Pc_{holo}/PSI$  as well as the different controls presented here, allow dissecting the contribution of the redox center and the surrounding protein scaffold to the interprotein charge exchange, and provide insights into the mechanism of interprotein ETp and ET. In particular, we associate the lower  $\Delta G$  of  $Pc_{holo}/PSI$  compared to  $Pc_{apo}/PSI$  to charge localization induced by the redox center. In trapped multi-heme cytochrome,<sup>60</sup> spatial confinement of high valence band states of the Fe orbitals is responsible for its low electronic coupling and thus poor contribution to the current. Also, the conductance histogram of  $Pc_{holo}/PSI$  displays a narrower distribution than  $Pc_{apo}/PSI$ , suggesting that interprotein ET pathways of the complex are dominated or “funneled” by specific through-Cu pathways, whereas in  $Pc_{apo}/PSI$  multiple and non-preferential ETp pathways through the protein matrix are available, leading to more spread conductance values. In any case, such pathways are built in the protein structure prior to metal binding, which appears to fine-tune them. These adjustments include the small but significant increase in  $\beta$  upon copper binding, corresponding to a decrease in the spatial span of the current between PSI and Pc (Figure 3). We tentatively associate these three differences in  $Pc_{apo}/PSI$  with respect to  $Pc_{holo}/PSI$  (lower  $\beta$ , higher  $\Delta G$ , and wider  $\Delta G$  distribution) to the metal-induced charge localization<sup>60</sup> and its effects on electronic coupling between electron acceptor and donor. Alternatively, the rigidity induced by the  $Cu^{2+}$  atom observed for azurin<sup>38</sup> is also expected in Pc, and it might restrict the allowed conformations and thus the possible ET pathways with PSI. This view is supported by the pathways calculation performed between bacterial reaction center and cytochrome *c*,<sup>57</sup> revealing that structure fluctuations have a significant impact on the overall ET rate of their encounter complex.

## Conclusions

In summary, we have characterized the remote and complex-bound ETp between single protein pair complexes of the photosynthetic electron transport chain by measuring the distance dependence and conductance of interprotein charge exchange between suitably oriented PSI and Pc. Using current-distance and blinking techniques in ECSTS, we respectively assessed the spatial span of the protein charge exchange as well as the formation of spontaneous protein junctions. We evaluated charge exchange distances for individual proteins and between the cognate protein pairs. Current-distance measurements reveal that, in ECSTS configuration, PSI and Pc proteins are capable of exchanging charge over several nm through the aqueous solution, either individually against a gold electrode, or in the Pc/PSI configuration. The copper ion in Pc enlarged the spatial span distance between Pc and a peptide functionalized electrode when compared to the non-redox  $Pc_{apo}$ . Interestingly, the presence of the copper ion in Pc diminished the charge exchange distance with the cognate PSI for a bias that favors the electrons flow from Pc to PSI, as it occurs in the photosynthetic electron transport chain. We therefore demonstrate that charge exchange between Pc and PSI can occur at long distances through the aqueous solution, and that Cu-less  $Pc_{apo}$  can sustain interprotein ETp with PSI at the single protein level despite the absence of redox activity.

Additionally, as probe and sample electrodes are functionalized with Pc and PSI respectively, we detect conductance blinks associated to the spontaneous formation of a molecular junction with a typical duration of  $\approx 6$  ms. This time scale is consistent with the Pc/PSI transient complex formation reported by bulk measurements. The conductance change  $\Delta G$ , measured for  $Pc_{\text{holo}}/PSI$  shows a lower value and a narrower distribution with respect to  $Pc_{\text{apo}}/PSI$ . In addition, a lower conductance blinking feature with a typical time decay of  $\approx 1$  ms was also observed, regardless the presence of the copper ion in the Pc. The conductance and duration of these blinking events suggest that they are related to transient configuration of water molecules leading to localized electronic states<sup>51</sup> that could mediate interprotein ET.<sup>53–56</sup> The narrow conductance distribution of  $Pc_{\text{holo}}/PSI$  compared to  $Pc_{\text{apo}}/PSI$  supports the idea of multiple and non-preferential ETp pathways through the protein matrix that are “funneled” to specific pathways through the Cu center in the natural redox active protein. This suggests a role of the redox center in fine tuning the interprotein ETp.

Our results extend the study of protein ETp to the interprotein domain and allow to dissect the contribution of the redox center in Pc by direct comparison between  $Pc_{\text{apo}}/PSI$  and  $Pc_{\text{holo}}/PSI$ . In particular, lower  $\beta$ , higher  $\Delta G$ , and wider  $\Delta G$  distribution are measured for Cu-less  $Pc_{\text{apo}}/PSI$ . We conclude that the protein matrix is sufficient to sustain long distance charge transport through the aqueous solution between  $Pc_{\text{apo}}$  and PSI as well as through the Pc/PSI transition complex, and we identify an additional role of the redox ion as regulator of the conductance, energetic distribution, and spatial span of the current.

## Methods

### *PSI-LHCI complexes purification*

Whole PSI-LHCI complexes (referred simply as PSI throughout the manuscript) were extracted from *Arabidopsis thaliana* plants (*Arabidopsis* Col-0) grown under white light at  $120 \mu\text{mol photons}\cdot\text{m}^{-2}\cdot\text{s}^{-1}$ , 12 hr/12 hr day/night cycles, for 5 weeks at 23 °C. Sucrose gradients were employed to purify PSI-LHCI complexes from thylakoid membranes isolated from *Arabidopsis* leaves as it has been previously described.<sup>61,62</sup> In particular, 350  $\mu\text{g}$  Chl thylakoid were diluted to  $0.5 \text{ mg Chl}\cdot\text{ml}^{-1}$  in EDTA 5 mM, HEPES 10 mM, pH 7.5 and solubilized with detergent solution (1%  $\alpha$ -decylmaltoside ( $\alpha$ -DM) in HEPES 10 mM, pH 7.5) for 10 min. Following solubilization, the sample was centrifuged at  $12\,000 \times g$  for 10 min discarding insolubilized material. The resulting solution was loaded in sucrose gradients prepared by freeze and thaw method (sucrose 500 mM, HEPES 20 mM, pH 7.5, 0.06%  $\alpha$ -DM) centrifuged for 16 h at 4 °C at  $160\,000 \times g$ . PSI-LHCI complexes were collected with a syringe.

### *Plastocyanin mutant expression and purification*

The mutant Pc-SH gene cloned into a pET-3a plasmid (pET-3a-PcSH) was used to transform *E. coli* BL21. The Pc-SH mutant (A121C) has three extra residues at its C-terminal (Thr-Cys-Gly). *E. coli* BL21 transformed with plasmid pET-3a-PcSH were grown in 2xYT medium supplemented with  $100 \mu\text{g}\cdot\text{ml}^{-1}$  of ampicillin at 37 °C until an OD600 of approximately 0.8 was reached. The expression of Pc-SH was induced by adding isopropyl thio- $\beta$ -D-galactoside (IPTG) 0.3 mM for 4 h, shaking at 220 rpm and 28 °C. Cells were harvested by centrifugation (7 000 rpm), suspended in MES buffer 10 mM, pH 6.5, and disrupted by sonication. The suspension was centrifuged for 1 hour at 20 000 rpm. The soluble fraction was loaded onto an anion exchange column (HiTrap® Q, Cytiva). A linear NaCl gradient (0–300 mM) in MES buffer 10 mM, pH 6.5, was used to elute Pc-SH. Subsequently, the protein-containing fractions were pooled and loaded onto a size exclusion column (Superdex® 75 10/300, Cytiva). Pc-SH purity was analyzed by SDS-PAGE stained with one-step blue® protein gel stain. The pure protein-containing

fractions were pooled, and glycerol was added to 40% v/v. The Pc-SH was stored at  $-20\text{ }^{\circ}\text{C}$  until the experiments were performed. Pc-SH mutant was purified in a Cu-less form (apo). To avoid the oxidation reaction between a cysteine residue of the Pc mutant and  $\text{Cu}^{2+}$ , apo Pc-SH ( $\text{Pc}_{\text{apo}}$ ) was directly bound to the Au STM probe or electrode. For the experiments with  $\text{Pc}_{\text{holo}}$ , the  $\text{Pc}_{\text{apo}}$  bound to the probe was incubated with fresh  $\text{Cu}^{2+}$  solution ( $\text{CuSO}_4$ , 50 mM) for 1 h at room temperature to bind  $\text{Cu}^{2+}$  (see below).

#### *Sample Preparation: PSI-pIQAcys-Au electrodes*

Prior to peptide incubation, Au[111] single-crystal electrodes of 10 mm diameter and 1 mm thickness (MaTeck) were electrochemically polished in  $\text{H}_2\text{SO}_4$ , flame annealed and cooled in Ar atmosphere. 100  $\mu\text{L}$  of PSI linker peptide pIQAcys solution 0.1 mM in  $\text{CH}_3\text{COONa}$  buffer 50 mM pH 4.5 was incubated for 30 min at room temperature. After peptide incubation, samples were gently rinsed with phosphate buffer saline (PBS) 50 mM, pH 7.4 (working buffer). 5  $\mu\text{L}$  of PSI samples ( $\text{OD}\sim 20$ ) were diluted in 45  $\mu\text{L}$  of PBS buffer for overnight incubation at  $4\text{ }^{\circ}\text{C}$ . After incubation, buffer was gently exchanged with PBS PSI-free buffer to elute unbound complexes. In a previous work, PSI-pIQAcys-Au functionalization was characterized with ECSTM and AFM and with cyclic voltammetry (CV) to define a working electrochemical window  $[-200, +300]$  mV/SSC where PSI complexes are photo-active<sup>40</sup>. Prior to ECSTM experiments, PSI activity was tested by measuring its photocurrent response to 690 nm irradiation in photo-chronoamperometry experiments at  $-100$  mV/SSC.

#### *Sample Preparation: $\text{Pc}_{\text{apo/holo}}$ -Au electrodes and $\text{Pc}_{\text{apo/holo}}$ -Au ECSTM probes*

Pc incubation for Au electrodes and ECSTM is similar: in the former 50  $\mu\text{L}$  of Pc-SH sample  $1\text{ mg}\cdot\text{mL}^{-1}$  in ammonium acetate buffer 50 mM pH 4.5 were incubated in freshly annealed Au[111] electrodes (see above). For probes, six ECSTM Au probes (see preparation method below) were placed in a polydimethylsiloxane (PDMS) coated petri dish around a 100  $\mu\text{L}$  drop of  $\text{Pc}_{\text{apo}}$ -SH  $1\text{ mg}\cdot\text{mL}^{-1}$  in ammonium acetate buffer allowing to soak all probe tips. After 1 h incubation at  $4\text{ }^{\circ}\text{C}$ , probes or electrodes were rinsed with MES buffer to remove unbound proteins. After rinsing,  $\text{Pc}_{\text{apo}}$ -SH samples were ready to use.  $\text{Pc}_{\text{holo}}$ -SH was further incubated for 1 h at  $4\text{ }^{\circ}\text{C}$  in 2-(*N*-morpholino)ethanesulfonic acid solution (MES) buffer 5 mM pH 5.5, containing 100 mM of  $\text{CuSO}_4$ . After rinsing with MES buffer, Au electrodes or probes are ready for cyclic voltammetry or ECSTS spectroscopy experiments respectively.

#### *ECSTM probes*

ECSTM probes were fabricated from  $\varnothing$  0.5 mm Au 99% wire (Mateck), mechanically cut with sharp handheld steel wire cutter. Probe holder was modified with a  $\varnothing$  0.6 mm hypodermic needle Microlance<sup>TM</sup> (BD) steel tube to accommodate thicker probes for enhanced mechanical and thermal stability. Probes were coated twice with Apiezon<sup>TM</sup> wax heated up to  $\sim 120\text{ }^{\circ}\text{C}$  in a home-built heat-coating applicator.

#### *Cyclic voltammetry*

Electrochemical measurements were carried out with a potentiostat PGSTAT 302N (Metrohm Autolab). CV experiments were performed in three-electrode cell used for ECSTM experiments. The cell includes (i) reference electrode based on a miniaturized ultralow leakage membrane Ag/AgCl (SSC) electrode filled with 3M KCl (World Precision Instruments) (ii) counter electrode made of  $\varnothing$  0.25 mm Pt80/Ir20 wire (Advent) (iii) working electrode of monocrystalline Au[111] coated with  $\text{Pc}_{\text{apo/holo}}$ -SH (see preparation above). CV were run between  $-100$  and  $300$  mV/SSC at a scan rate of  $5\text{ mV}\cdot\text{s}^{-1}$ . Experiments were carried out in working buffer (PBS 50 mM, pH 4.5) at room temperature.  $\text{Pc}_{\text{holo}}$  CV

was performed on the same  $Pc_{apo}$  after  $CuSO_4$  incubation and thorough rinsing. Cell and all glass material used for preparation of solutions were cleaned with piranha solution (7:3  $H_2SO_4/H_2O_2$  (30%) by volume). **Caution: Piranha solution should be handled with extreme caution.**

#### *Electrochemical scanning tunneling spectroscopy (ECSTS) measurements*

All experiments were performed with a PicoSPM microscope head and a PicoStat bipotentiostat (Agilent) controlled by Dulcinea electronics (Nanotec Electrónica) using the WSxM 4 software.<sup>63</sup> Bipotentiostat allows adjusting sample and probe potentials,  $U_s$  and  $U_p$ , independently. A homemade electrochemical cell described above was used for CV and ECSTM experiments.

The ECSTM head was placed on a passive mechanical vibration isolation system (900 kg block suspended by 3 metal springs of 4 m length and  $\sim 1.7 \text{ kN}\cdot\text{m}^{-1}$  each) achieving a 0.3 Hz cut-off frequency, and a decrease of -40 dB in vertical seismic acceleration. The damping rate was reduced to  $\sim 1 \text{ min}^{-1}$  by stuffing the springs with steel wool. A cylindrical cover made of 1 cm thick neoprene provided acoustic damping to the ECSTM head during experiments.

Current-distance  $I(z)$  curves were acquired by departing from a set-point current fixed at 0.3 nA. For these experiments, we used only probes displaying leakage current below 8 pA. The current feedback-loop was switched off and the probe electrode was retracted 10 nm at  $40 \text{ nm}\cdot\text{s}^{-1}$ . Afterwards, the probe was approached again, and the current-distance feedback loop was reestablished for 100 ms before retracting again. 1000  $I(z)$  curves were recorded for each sample and two independent samples were prepared and measured for each condition. To minimize drift artifacts,  $I(z)$  curves departing with a current deviation higher than 10% of the initial set point were discarded. For all current-distance experiments, the probe potential was set to 100 mV/SSC, near the  $Pc$  redox mid-point. The sample potential was set to 0 mV/SCC and 200 mV/SSC yielding +100 and -100 mV of bias voltage, forcing the electron transfer from sample to probe and *vice versa*, respectively. The spatial span of the interprotein charge exchange process was quantified by fitting  $I(z)$  curves with a double exponential model described previously, separately fitting the current-distance rate for short and long distance.<sup>40</sup>  $I(z)$  curve double-exponential fitting routine was implemented in *R* software and is available at [https://github.com/Mlopeorti/Tunnel\\_current\\_2exponential\\_fitter](https://github.com/Mlopeorti/Tunnel_current_2exponential_fitter). The short distance regime has been reported to be affected by the electric double layer deployed in the vicinity of the electrode interface.<sup>41,42</sup> Thus, to avoid artifacts, protein charge-exchange distance results and discussion is based on the long-distance regime. The  $\beta$  values in the short distance regime ( $\beta_0$ ) and the distance for regime change ( $Z_0$ ) for all the experimental conditions are shown in Supplementary Figure 7 and 8 respectively.

Histograms showing the distribution of  $\beta$  values were analyzed and represented with Matlab 2021 (The MathWorks Inc.). The distribution of  $\beta$  values was fit around the maximum frequency with a normal distribution, reporting the value as the mean value  $\pm$  the standard deviation of the distribution, that is  $\langle\beta\rangle \pm \sigma(\beta)$ .

For blinking experiments, we used a NI-DAQmx and BNC-2110 acquisition card controlled by Labview (National Instruments). After a period of mechanical stabilization, the STM probe was placed to achieve a set-point current of 1 nA, until the feedback is turned off. Current versus time traces were then recorded in three-second bouts during a total time of several hours. Current blinks were observed as current transients in the form of telegraphic noise (Fig. 2a). The current increment of the blink  $\Delta I$ , was transformed to conductance values using  $G = \Delta I_{\text{blink}}/U_{\text{bias}}$ .

At least two independent experiments were conducted in each case, adding up to  $n = 4110$  for PSI- $Pc_{apo}$  and  $n = 4216$  for  $Pc_{holo}$ /PSI blinking events, automatically recognized using a customized current

threshold strategy (see supplementary figure 4) implemented in Matlab 2021 (The MathWorks Inc.). Data was analyzed, pooling blinking events in a common time and conductance origin to build a two-dimensional histogram with  $\Delta G$  in y-axis  $\Delta t$  in x-axis. Conductance peaks, marked with stars and open circles in the side panel of figure 4b, were fit with a normal distribution. The reported values correspond to the mean value  $\pm$  the standard error of the mean. For the time decay of the blinking duration, we obtained the time constant and their associated error by linear regression of the natural logarithm of the number of counts for short time regime ( $\Delta t < 2$  ms) and long time regime ( $\Delta t > 5$  ms).

## Acknowledgements

We thank Roberta Croce and Chen Hu for providing PSI-LHCI samples and for their comments on the manuscript. We thank G. W. Canters, S. Cannistraro, and L. Andolfi for the kind gift of Pc clones. We also thank everybody involved in the development and set-up of the anti-vibratory system: Iñaki Bahamonde (HierroK), Lourdes Sánchez (Piedra Artificial), David Izquierdo (Core Facilities IBEC), Anna Mezquita (Parc Científic de Barcelona), Jaume Clapés (Applied Geophysics Service of the Universitat Politècnica de Catalunya). R.Z. was supported by National Agency for Research and Development (ANID)/Scholarship Program POSTDOCTORADO BECAS CHILE/2018-74190117. This research received funding from the European Union Research and Innovation Programme Horizon 2020 – HBP SG3 (grant agreement No. 945539), DEEPER (ICT-36-2020, grant agreement No. 101016787), and financial support from Agency for Management of University and Research Grants (CERCA Programme; 2021-SGR-1410 project), Ministry of Science and Innovation DEEP RED grant No. PID2019-111493RB-I00 funded by MCIN/AEI/10.13039/501100011033, the Commission for Universities and Research of the Department of Innovation, Universities, and Enterprise of the Generalitat de Catalunya -AGAUR-(IU16-011508) and cofinanced by the European Union Regional Development Fund within the framework of the ERDF/FEDER Operational Program of Catalonia 2014 – 2020 with a grant of 50% of total eligible cost. This research was also supported by CIBER (Consortio Centro de Investigación Biomédica en Red, CB06/01/0081), Instituto de Salud Carlos III, Ministerio de Ciencia e Innovación.

## References

1. Derek Bendall. *Protein Electron Transfer*. (Garland Science, 1996).
2. Winkler, J. R. & Gray, H. B. Electron flow through metalloproteins. *Chem Rev* **114**, 3369–3380 (2014).
3. Chitnis, P. R. Photosystem I: Function and Physiology. *Annu Rev Plant Physiol Plant Mol Biol* **52**, 593–626 (2001).
4. Cahen, D., Pecht, I. & Sheves, M. What Can We Learn from Protein-Based Electron Transport Junctions? *Journal of Physical Chemistry Letters* **12**, 11598–11603 (2021).
5. Bostick, C. D., Mukhopadhyay, S., Sheves, M., Cahen, D. & Lederman, D. Protein bioelectronics : a review of what we do and do not know. *Reports on Progress in Physics* **81(2)**, 1–150 (2018).
6. Zhang, B., Song, W., Brown, J., Nemanich, R. & Lindsay, S. Electronic Conductance Resonance in Non-Redox-Active Proteins. *J Am Chem Soc* **142**, 6432–6438 (2020).
7. Zhang, B. *et al.* Engineering an Enzyme for Direct Electrical Monitoring of Activity. *ACS Nano* **14**, 1360–1368 (2020).

8. Zhang, B. *et al.* Role of contacts in long-range protein conductance. *Proc Natl Acad Sci U S A* **116**, 5886–5891 (2019).
9. Zhang, B. *et al.* Observation of giant conductance fluctuations in a protein. *Nano Futures* **1**, 035002 (2017).
10. Garg, K. *et al.* Direct evidence for heme-assisted solid-state electronic conduction in multi-heme: C -type cytochromes. *Chem Sci* **9**, 7304–7310 (2018).
11. Kayser, B. *et al.* Solid-State Electron Transport via the Protein Azurin is Temperature-Independent Down to 4 K. *J Phys Chem Lett* **11**, 144–151 (2020).
12. Guo, C. *et al.* Tuning electronic transport via hepta-alanine peptides junction by tryptophan doping. *Proc Natl Acad Sci U S A* **113**, 10785–10790 (2016).
13. Yu, X. *et al.* Insights into Solid-State Electron Transport through Proteins from Inelastic Tunneling Spectroscopy: The Case of Azurin. *ACS Nano* **9**, 9955–9963 (2015).
14. Ron, I. *et al.* Proteins as electronic materials: Electron transport through solid-state protein monolayer junctions. *J Am Chem Soc* **132**, 4131–4140 (2010).
15. Amdursky, N. *et al.* Electronic Transport via Proteins. *Advanced Materials* **26**, 7142–7161 (2014).
16. Mukhopadhyay, S. *et al.* Solid-State Protein Junctions: Cross-Laboratory Study Shows Preservation of Mechanism at Varying Electronic Coupling. *iScience* **23**, 101099 (2020).
17. Lindsay, S. Ubiquitous electron transport in non-electron transfer proteins. *Life* **10**, 72 (2020).
18. Zhang, B., Ryan, E., Wang, X., Song, W. & Lindsay, S. Electronic Transport in Molecular Wires of Precisely Controlled Length Built from Modular Proteins. *ACS Nano* **16**, 1671–1680 (2022).
19. Lagunas, A. *et al.* Long distance electron transfer through the aqueous solution between redox partner proteins. *Nat Commun* **9**, 3–9 (2018).
20. Alexandre Gomila *et al.* Phosphorylation disrupts long-distance electron transport in cytochrome c. *Nat Commun* **13**, 7100 (2022).
21. Pérez-Mejías, G., Díaz-Quintana, A., Guerra-Castellano, A., Díaz-Moreno, I. & de la Rosa, M. A. Novel insights into the mechanism of electron transfer in mitochondrial cytochrome c. *Coord Chem Rev* **450**, (2022).
22. Hope, A. B. Electron transfers amongst cytochrome f, plastocyanin and photosystem I: Kinetics and mechanisms. *Biochim Biophys Acta Bioenerg* **1456**, 5–26 (2000).
23. Sommer, F., Drepper, F. & Hippler, M. The luminal helix I of PsaB is essential for recognition of plastocyanin or cytochrome c6 and fast electron transfer to photosystem I in *Chlamydomonas reinhardtii*. *Journal of Biological Chemistry* **277**, 6573–6581 (2002).
24. Drepper, F., Hippler, M., Nitschke, W. & Haehnel, W. Binding dynamics and electron transfer between plastocyanin and photosystem I. *Biochemistry* **35**, 1282–1295 (1996).

25. Sommer, F., Drepper, F., Haehnell, W. & Hippler, M. The Hydrophobic Recognition Site Formed by Residues PsaA-Trp651 and PsaB-Trp627 of Photosystem I in *Chlamydomonas reinhardtii* Confers Distinct Selectivity for Binding of Plastocyanin and Cytochrome c 6. *Journal of Biological Chemistry* **279**, 20009–20017 (2004).
26. Kuhlert, S., Drepper, F., Fufezan, C., Sommer, F. & Hippler, M. Residues PsaB Asp612 and PsaB Glu613 of photosystem i confer pH-dependent binding of plastocyanin and cytochrome c 6. *Biochemistry* **51**, 7297–7303 (2012).
27. Ha, T. Q., Planje, I. J., White, J. R. G., Aragonès, A. C. & Díez-Pérez, I. Charge transport at the protein–electrode interface in the emerging field of biomolecular electronics. *Curr Opin Electrochem* **28**, 100734 (2021).
28. Salvatore, P. *et al.* Electrochemistry of single metalloprotein and DNA-based molecules at Au(111) electrode surfaces. *ChemPhysChem* **14**, 2101–2111 (2013).
29. Ricarda Höhnera *et al.* Plastocyanin is the long-range electron carrier between photosystem II and photosystem I in plants. *PNAS* **117**, (2020).
30. Mamedov, M. D., Mamedova, A. A., Chamorovsky, S. K. & Semenov, A. Y. Electrogenic reduction of the primary electron donor P700 by plastocyanin in photosystem I complexes. *FEBS Lett* **500**, 172–176 (2001).
31. Hervás, M., Navarro, J. A., Díaz, A. & De La Rosa, M. A. A Comparative Thermodynamic Analysis by Laser-Flash Absorption Spectroscopy of Photosystem I Reduction by Plastocyanin and Cytochrome c 6 in *Anabaena* PCC 7119, *Synechocystis* PCC 6803, and *Spinach*. *Biochemistry* **35**, 2693–2698 (1996).
32. Haehnel, W. *et al.* Electron transfer from plastocyanin to photosystem I. *EMBO Journal* **13**, 1028–1038 (1994).
33. Zamora, R. A. *et al.* Light- and Redox-Dependent Force Spectroscopy Reveals that the Interaction between Plastocyanin and Plant Photosystem I Is Favored when One Partner Is Ready for Electron Transfer. *ACS Nano* **16**, 15155–15169 (2022).
34. Garrett, T. P. J., Clingeffer, D. J., Guss, J. M., Rogers, S. J. & Freeman, H. C. The Crystal Structure of Poplar Apoplastocyanin at 1.8-Å Resolution. *The American Society of Biological Chemist* **0**, 2822–2825 (1984).
35. Romero-Muñiz, C. *et al.* The Role of Metal Ions in the Electron Transport through Azurin-Based Junctions. *Applied Sciences* **11**, 3732 (2021).
36. Nar, H., Messerschmidt, A., Huber, R., van de Kamp, M. & Canters, G. W. Crystal structure of *Pseudomonas aeruginosa* apo-azurin at 1.85 Å resolution. *FEBS Lett* **306**, 119–124 (1992).
37. Nar, H., Messerschmidt, A., Huber, R., van de Kamp, M. & Canters, G. W. Crystal structure analysis of oxidized *Pseudomonas aeruginosa* azurin at pH 5.5 and pH 9.0. *J Mol Biol* **221**, 765–772 (1991).
38. Giannotti, M. I. *et al.* Direct Measurement of the Nanomechanical Stability of a Redox Protein Active Site and Its Dependence upon Metal Binding. *J Phys Chem B* **119**, 12050–12058 (2015).

39. Gordiichuk, P. *et al.* Orientation and Incorporation of Photosystem I in Bioelectronics Devices Enabled by Phage Display. *Advanced Science* **4**, (2017).
40. López-Ortiz, M. *et al.* Distance and Potential Dependence of Charge Transport Through the Reaction Center of Individual Photosynthetic Complexes. *Small* **18**, (2022).
41. Wigginton, N. S., Rosso, K. M., Stack, A. G. & Hochella, M. F. Long-range electron transfer across cytochrome-hematite ( $\alpha$ -Fe<sub>2</sub>O<sub>3</sub>) interfaces. *Journal of Physical Chemistry C* **113**, 2096–2103 (2009).
42. Artés, J. M., Díez-Pérez, I., Sanz, F. & Gorostiza, P. Direct measurement of electron transfer distance decay constants of single redox proteins by electrochemical tunneling spectroscopy. *ACS Nano* **5**, 2060–2066 (2011).
43. He, J., Lin, L., Zhang, P. & Lindsay, S. Identification of DNA Basepairing via Tunnel-Current Decay. *Nano Lett* **7**, 3854–3858 (2007).
44. López-Martínez, M. *et al.* Electrochemically Gated Long-Distance Charge Transport in Photosystem I. *Angewandte Chemie - International Edition* **58**, 13280–13284 (2019).
45. Díez-Pérez, I. *et al.* Rectification and stability of a single molecular diode with controlled orientation. *Nat Chem* **1**, 635–641 (2009).
46. Artés, J. M., López-Martínez, M., Díez-Pérez, I., Sanz, F. & Gorostiza, P. Conductance switching in single wired redox proteins. *Small* **10**, 2537–2541 (2014).
47. Ruiz, M. P. *et al.* Bioengineering a Single-Protein Junction. *J Am Chem Soc* **139**, 15337–15346 (2017).
48. Aragonès, A. C. *et al.* Single-molecule electrical contacts on silicon electrodes under ambient conditions. *Nat Commun* **8**, 1–8 (2017).
49. Tang, L. *et al.* Measuring conductance switching in single proteins using quantum tunneling. *Sci. Adv* **8**, 8149 (2022).
50. Artés, J. M., Díez-Pérez, I. & Gorostiza, P. Transistor-like behavior of single metalloprotein junctions. *Nano Lett* **12**, 2679–2684 (2012).
51. Xiang, L. *et al.* Conductance and Configuration of Molecular Gold-Water-Gold Junctions under Electric Fields. *Matter* **3**, 166–179 (2020).
52. Boussaad, S. *et al.* Discrete tunneling current fluctuations in metal-water-metal tunnel junctions. *Journal of Chemical Physics* **118**, 8891–8897 (2003).
53. Zhang, B. *et al.* Observation of giant conductance fluctuations in a protein. *Nano Futures* vol. 1 Preprint at (2017).
54. Michaeli, K., Beratan, D. N., Waldeck, D. H. & Naaman, R. Voltage-induced long-range coherent electron transfer through organic molecules. *Proc Natl Acad Sci U S A* **116**, 5931–5936 (2019).
55. de La Lande, A., Babcock, N. S., Řezáč, J., Sanders, B. C. & Salahub, D. R. Surface residues dynamically organize water bridges to enhance electron transfer between proteins. *Proc Natl Acad Sci U S A* **107**, 11799–11804 (2010).

56. Lin, J., Balabin, I. A. & Beratan, D. N. The nature of aqueous tunneling pathways between electron-transfer proteins. *Science (1979)* **310**, 1311–1313 (2005).
57. Miyashita, O., Okamura, M. Y. & Onuchic, J. N. Interprotein electron transfer from cytochrome c 2 to photosynthetic reaction center: Tunneling across an aqueous interface. *Proceedings of the National Academy of Sciences* **102**, 3558–3563 (2005).
58. Halbritter, J., Repphun, G., Vinzelberg, S., Staikov, G & Lorenz, W. J. Tunneling mechanism in electrochemical STM. *Pergamon Elctrochimica Am* **40**, 1995 (1994).
59. Romero-Muñiz, C. *et al.* Can Electron Transport through a Blue-Copper Azurin Be Coherent? An Ab Initio Study. *The Journal of Physical Chemistry C* **125**, 1693–1702 (2021).
60. Futera, Z. *et al.* Coherent Electron Transport across a 3 nm Bioelectronic Junction Made of Multi-Heme Proteins. *J Phys Chem Lett* **11**, 9766–9774 (2020).
61. Xu, P., Tian, L., Kloz, M. & Croce, R. Molecular insights into Zeaxanthin-dependent quenching in higher plants. *Sci Rep* **5**, 1–10 (2015).
62. Caffarri, S., Kouřil, R., Kereiče, S., Boekema, E. J. & Croce, R. Functional architecture of higher plant photosystem II supercomplexes. *EMBO Journal* **28**, 3052–3063 (2009).
63. Horcas, I. *et al.* WSXM: A software for scanning probe microscopy and a tool for nanotechnology. *Review of Scientific Instruments* **78**, 013705 (2007).